Optics Letters

Amplification of femtosecond pulses based on $\chi^{(3)}$ nonlinear susceptibility in MgO

Chathurangani Jayalath Arachchige, Jacob A. Stephen, and T. J. Hammond*

Department of Physics, University of Windsor, 401 Sunset Dr., Windsor, Ontario N9B 3P4, Canada
*Corresponding author: thammond@uwindsor.ca

We experimentally demonstrate large, widely tunable gain using Kerr instability amplification in MgO. By pumping the crystal near optical damage at 1.4×10^{13} W/cm² by a femtosecond Ti:sapphire laser, we amplify visible and near-infrared pulses by factors >5000 or a gain $g \approx 17/$ mm. We temporally characterize the pulses to show that they are 42 fs in duration, much shorter than the pump pulse. In the non-collinear setup, the angle between the pump and seed selects the amplified wavelength, where we find certain angles amplify both the visible and near-infrared simultaneously. We find that near the maximum pumping intensities, higher-order nonlinearities may play a role in the amplification process. © 2021 Optical Society of America

https://doi.org/10.1364/OL.437749

The workhorse for ultrafast optics for over two decades has been the mode-locked Ti:sapphire laser oscillator that uses the $\chi^{(3)}$ Kerr response to produce nanojoule femtosecond (1 fs = 10^{-15} s) pulses in the near-infrared (IR) [1,2]. Amplification of these fs pulses in a chirped-pulse amplification (CPA) scheme [3], pumped by a nanosecond Q-switched laser increases the pulse energy by many orders to magnitude, from several millijoules for commercial systems [4], up to several Joules for bespoke table-top setups [5,6]. Spectral compensators condition the seed spectrum to increase the amplified pulse bandwidth to support shorter pulses [5,7].

These amplified fs Ti:sapphire lasers are now the energy source for many of the next generation light sources. Optical parametric amplification (OPA) produces fs pulses spectrally tunable from the near- to mid-IR [8]. These OPAs typically use a non-centrosymmetric $\chi^{(2)}$ nonlinear crystal to split a fs pump pulse into a signal and idler of lower energy. Non-collinear phase-matching OPA (NOPA) [9], chirped-pulse OPA (OPCPA) [10], Fourier OPA (FOPA) [11] are some of the techniques that increase the amplified bandwidth. Because parametric processes do not store energy in the crystal, amplification only occurs while the pump pulse interacts with the gain medium, improving pulse contrast necessary for high power systems [12,13].

Recently, amplification from Kerr instability exploiting the $\chi^{(3)}$ nonlinearity was reported to amplify fs pulses over a broad spectrum [14]. Because all materials possess $\chi^{(3)}$ nonlinear susceptibility, Kerr instability amplification (KIA) has the potential

to be a more versatile amplifier for widely tunable fs pulses, such as amplification in the UV or THz [15]. KIA depends on the nonlinear index of refraction [16],

$$n_2 = \frac{3}{4\epsilon_0 n_0^2 c} \chi^{(3)}(-\omega; \omega, \omega, -\omega), \quad \textbf{(1)}$$

where $n_0 = n(\omega_0)$ is the linear index of refraction evaluated at the central frequency. However, the maximum nonlinear response of the material depends on $n_2 I_0$, where I_0 is the peak intensity. That is, the combination of both high n_2 and I_0 leads to the maximum potential gain. Thus, although YAG ($n_2 = 6 \times 10^{-20}$ W/m²) and YVO₄ ($n_2 \approx 15 \times 10^{-20}$ W/m²) [17] have higher nonlinear indices of refraction than MgO ($n_2 = 4 \times 10^{-20}$ W/m²) [18], we found that the maximum intensity MgO withstands before breakdown is higher.

We show the setup of the experiment in Fig. 1(a). We take the output of a vertically polarized 1.5 mJ fs Ti:sapphire laser, and a CaF₂ window splits the beam in two arms: the seed and the pump. In the seed arm, we control the mode profile and the power using an iris (I_1), and we tightly focus the beam (lens $f_1 = 75$ mm) onto a 5 mm Al₂O₃ crystal to create a supercontinuum (SC), as shown in Fig. 1(b). We collimate and loosely focus this SC ($f_2 = 100$ mm), removing the quickly diverging
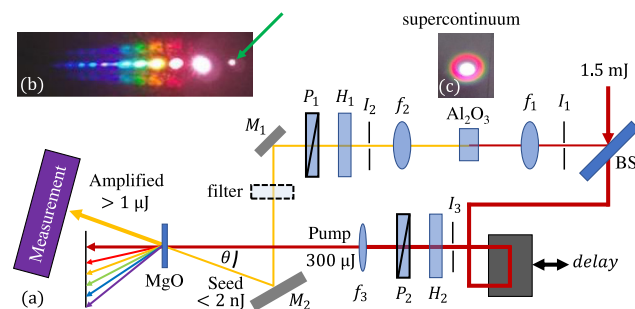

Fig. 1. (a) Experimental setup of the Kerr instability amplification scheme. The delay stage, along with mirrors M_1 and M_2, ensures spatial and temporal overlap of the pump and seed on the MgO crystal. We amplify the supercontinuum generated in 5 mm sapphire, spectrally filtering either the visible or IR portion. $H_{1,2}$, half-wave plate; $P_{1,2}$, polarizer; $f_{1,2,3}$, lens; $I_{1,2,3}$, iris; measurement is powermeter, FROG, spectrometer, or camera. (b) Supercontinuum seed generated in sapphire. (c) The multiple beams generated by the NDC4WM; green arrow indicates amplified beam.

portion of the beam with a second iris (I_2). We can control the seed power using a half-wave plate (H_1) and polarizer (P_1). We place either visible or infrared filters to transmit the seed frequency of interest, while blocking the residual fundamental beam. We direct the seed beam to the MgO optic using two mirrors (M_1, M_2) to control the overlap and relative angle, θ, of the seed and pump beams. The MgO crystal (from MTI Corporation) dimensions are 10 mm × 10 mm, and 0.5 mm thick (100 cut).

The manual delay stage in the pump arm controls the temporal overlap. The pump profile is slightly clipped with an iris (I_2) to control the beam size at the focus. We can also control the pump intensity with a half-wave plate (H_2) and polarizer (P_2). This beam is loosely focused on to the MgO crystal with a $f_3 = 500$ mm focal length lens, with the crystal placed just after the focus. With the beam waist at the crystal of 95 μm × 125 μm and pulse duration of 115 fs, the maximum peak intensity at the MgO crystal is estimated to be $1.4 \pm 0.1 \times 10^{13}$ W/cm^2 when the pump energy is 300 μJ, beyond which we find that the crystal quickly changes character and the amplified signal significantly degrades. Up to this maximum peak intensity, we find negligible damage to the optic over extended periods of time. This intensity is similar to the maximum intensity investigated in high harmonic generation in MgO [19–21].

When the near-IR seed and intense pump are overlapped with relative angle 4−9°, we observe a series of visible beamlets, which extend to the UV, as shown in Fig. 1(c). These beamlets are a result of non-degenerate cascaded four-wave mixing (NDC4WM) [22]. The amplified near-IR beam is indicated by the green arrow.

We now discuss the amplification of the seed pulse when it overlaps with the pump pulse, as shown in Fig. 2(a). We filter the seed spectrum with a visible or infrared filter to remove the presence of the dominating 785 nm portion of the spectrum. The long integration time required for the spectrometer (OceanOptics Flame-S) to properly characterize the weak seed amplitude would be saturated by this central wavelength, making it difficult to characterize the amplification. When we place a visible bandpass filter (bandpass 335–610 nm) in the SC, the weak seed pulse energy is <2.5 nJ, given by the light red curve. We define the amplification factor as the increase in peak counts in the spectrometer, taking the integration time of the amplified (10 ms) and seed (200 ms) beams. When the pump is present (dark red), the spectral peak increases by a factor >4000×,

which we define as the amplification factor. We replace this visible filter with an IR filter (longpass >880 nm) to observe the IR portion of the SC; we maintain the same seed–pump relative angle of 5.3°, but change the delay to find temporal overlap. We change the delay because the SC seed is chirped due to the self-phase modulation process and the dispersive optic elements between the sapphire and the MgO, and to compensate in the difference in optical thicknesses of the filters. We expect that with compressed few-cycle pulses, KIA will be able to amplify the entire spectrum. Although this infrared portion of the seed beam is weaker than in the visible, we achieve amplification >6000× leading to similar output amplitude. These amplification factors correspond to a gain of $g \approx 17$mm for the 0.5 mm optic. In the visible case, the transform limited pulse duration is 22 fs, and in the IR it is 35 fs. Because we observe large amplification in both the visible at 600 nm and the near-IR at 900 nm at the same relative angle of the seed and pump, we expect that using this non-collinear geometry will enable the amplification of broadband pulses.

We temporally characterize the amplified IR pulse with a home-built frequency resolved optical gating (FROG) measurement, as shown in Fig. 2(b). We measure a 42 fs full width at half-maximum (FWHM) pulse (dark solid blue), and find it has a residual 350 fs^2 of dispersion, as calculated by the quadratic phase dependence (red solid, right axis). We include the 115 fs FWHM pulse measured directly from the laser as reference (light dashed blue). We can measure amplified pulses with central wavelength 850–1000 nm with our setup, and we find that these pulses are consistently ∼1/3 the pulse duration of the pump laser, in agreement with the amplified pulses measured in [14]. Although this pulse duration can be explained by the highly nonlinear amplification scaling involved in Kerr instability, as shown in Fig. 3, optimizing the parameters to minimize the amplified pulse duration is the subject of future work.

In Fig. 3, we show the scaling of the amplified spectra with the pump and seed energy. We find that the visible [Fig. 3(a)] and IR amplified [Fig. 3(b)] spectra do not distort even in cases of high gain. The sudden change in the background at 150 μJ for the visible and 180 μJ for the IR is due to increasing the integration time. In Fig. 3(c), at low (<1.5 nJ) seed energy, we find that for both the visible and IR amplified beams the amplification factor follows a pump energy scaling of P^9 (dashed line) up to a saturation intensity, which is near the damage threshold for MgO. This scaling emphasizes the importance of peak intensity on the Kerr amplification process, and can explain the short amplified pulse duration. A seed pulse with the same Gaussian envelope as the pump, amplified with a scaling $P^9(t)$, leads to $\tau_a = \tau_p/3$, where $\tau_{a,p}$ are the durations of the amplified and seed pulses, respectively; a more involved model taking dispersion, beam walk-off, saturation, and initial seed chirp would increase τ_a.

The measured gain is significantly lower than predicted in the plane wave cw limit, but comparable to the finite beam and single-cycle theory [15]. This saturation has the benefit that the amplification process is stable against small fluctuations in the pump power. As expected, the amplified signal (blue), which we define as the total spectrometer counts, is proportional to the seed energy (black dash) at low energy, as shown in (d); the amplified signal diverges from the linear P^1 scaling at high seed energy (>1.5 nJ) also leading to a maximum amplified pulse energy. Saturation is caused by many effects, such as self-focusing induced wavefront distortion of the pump, cross talk
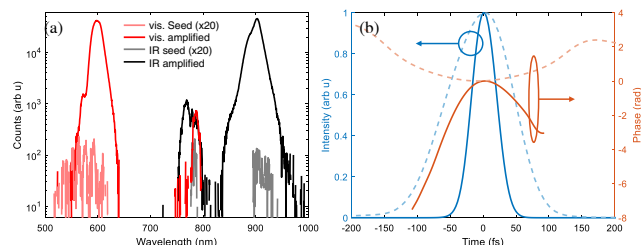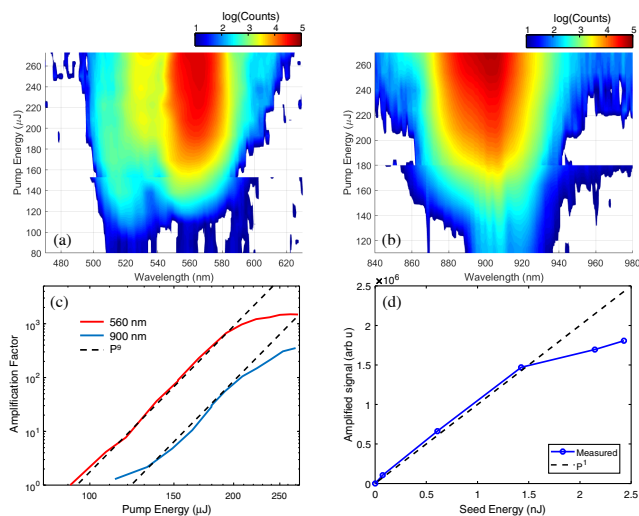

Fig. 2. (a) Amplified pulses centered at 590 nm (red) and 900 nm (black) integrated over 10 ms; seed supercontinuum spectra (light red and gray) filtered by appropriate spectral filters and integrated over 200 ms. The spectrum near 800 nm is a scattered pump. (b) Reconstructed FROG measurements of the pump pulse (amplitude, blue dash; phase, red dash) and amplified pulse at 880 nm (solid). The measured amplified pulse is 42 fs, much shorter than the 115 fs pump pulse.

Fig. 3. Amplified spectra in the (a) visible and (b) near-IR. (c) Both the visible and the near-IR exhibit P^9 amplification dependence on pump power until saturation. (d) The amplification factor is independent of small seed pulse energy; at higher seed energies, the amplification process can distort the pulse.

Fig. 4. Amplified spectra angle dependence of the near-IR seed.

Fig. 5. Seed beam shape when the seed arrives at the MgO (a) before and (b) simultaneously with the pump pulse, taken at 11° to avoid amplification. (c) The relative transmission factor of the seed beam without/with the pump pulse.

between the amplified pulse and the other beamlets, amplified pulse breakup, and complex nonlinear susceptibilities.

We can also tune the amplified spectrum by varying the relative angle of the seed and pump. Because KIA is a nonlinear process, phase-matching plays a role and requires a non-collinear geometry. Although phase-matching is automatically satisfied in KIA [14,15], we tune the relative seed–pump angle to match the transverse momentum for maximum gain, requiring a non-collinear geometry setup. A similar situation arises in conical emission, where an intense pump pulse filaments to create an angle-dependent SC spectrum, as shown in Fig. 1(c). However, conical emission grows out of noise, and in contrast, in KIA we seed the amplification process, which leads to a similar (but not necessarily the same) angular dependence.

Figure 4 shows the spectrometer counts for different relative angles. The spectral maxima for longer wavelengths decrease because of the limited bandwidth seed spectrum, geometrical overlap of the finite seed and pump beams, and wavelength dependence of gain [15]. For this measurement, we place our 880 nm low pass filter after the amplification process because scatter from the pump beam saturates the spectrometer at small angles. The uncertainty in the relative angle is ±0.3°. As we increase the relative angle, we can amplify longer wavelengths, but we find that beyond 9° we do not see significant amplification.

We investigate the effect of the pump beam on the visible portion of the seed beam in the near-field, as shown in Fig. 5. The relative angle between the seed and pump beam is 11°, and we do not observe amplification. We propagate only the seed beam and reimage the profile onto a CCD camera. The seed beam arriving at the MgO crystal is shown in Fig. 5(a), exhibiting a Gaussian beam profile. However, when the pump beam arrives at the crystal simultaneously with the seed [Fig. 5(b)], we observe that there is a significant decrease in the transmitted seed beam, indicating significant electronic modification by the pump beam. The relative decrease in the transmitted seed beam (that is, the transmitted beam intensity ratio of the seed without
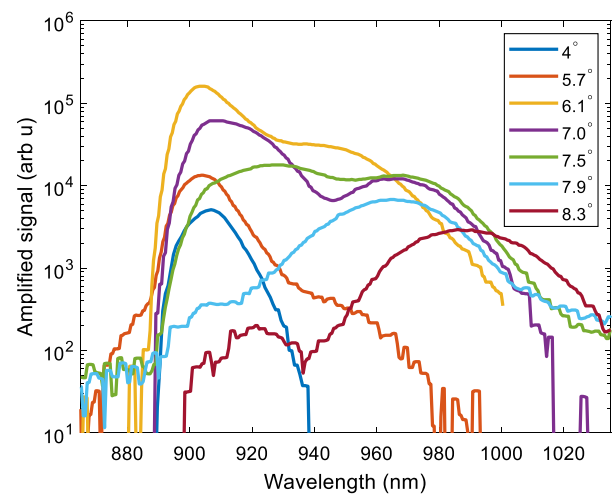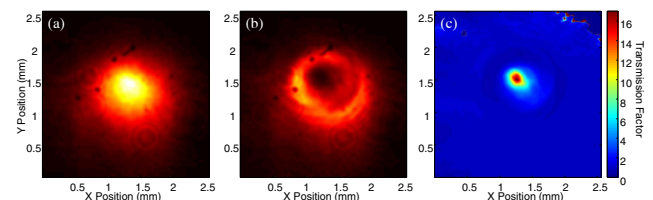
pump/with pump) is shown in Fig. 5(c), where the maximum is approximately a factor of 17. These transient excited states in the MgO may be further explored using this non-collinear technique to understand their nature and lifetime [23].

The value of $\chi^{(5)}$, to our knowledge, has not been previously reported for MgO, although it has been found to be complex in other materials [24]. Because MgO has been found to be a useful source for high harmonic generation under similar intensities and driving fields as observed here, these higher-order nonlinearities may play a role in the conversion efficiency and propagation of high-order harmonics. Techniques to characterize these higher-order nonlinearities have been developed [25,26]. With a photon energy of 1.58 eV and a bandgap of MgO of 7.8 eV [27], we expect five-photon absorption to play a role [28]. It may be that we are near a five-photon absorption resonance [29,30] and using a pump laser of longer wavelength (lower photon energy) may significantly alter this nonlinear response; it may be possible to more efficiently amplify fs pulses in MgO, and further investigation is required.

In conclusion, we investigated KIA in MgO. The extremely high P^9 power scaling will lead to an excellent pulse contrast for high power systems. Although MgO only has a moderate n_2 compared to other dielectrics, its ability to withstand high intensities without optical damage makes it a better candidate for amplification than YAG. Additionally, the multiphoton absorption process, although parasitic to the amplification process, greatly simplifies the seed and pump alignment, both spatially and temporally.

Disclosures. The authors declare no conflicts of interest.

Data Availability. Data underlying the results presented in this Letter are not publicly available at this time but may be obtained from the authors upon reasonable request.

REFERENCES

1. T. W. Hänsch, Rev. Mod. Phys. **78**, 1297 (2006).
2. J. L. Hall, Rev. Mod. Phys. **78**, 1279 (2006).
3. D. Strickland and G. Mourou, Opt. Commun. **56**, 219 (1985).
4. J. L. E. K. M. Dorney, D. D. Hickstein, N. J. Brooks, C. Gentry, C. Hernández-Garcia, D. Zusin, J. M. Shaw, Q. L. Nguyen, C. A. Mancuso, G. S. M. Jansen, S. Witte, H. C. Kapteyn, and M. M. Murnane, Optica **5**, 479 (2018).
5. S. Fourmaux, S. Payeur, S. Buffechoux, P. Lassonde, C. St-Pierre, F. Martin, and J. C. Kieffer, Opt. Express **19**, 8486 (2011).
6. E. Cunningham, Y. Wu, and Z. Chang, App. Phys. Lett. **107**, 201108 (2015).
7. J. Seres, A. Müller, E. Seres, K. O'Keeffe, M. Lenner, R. F. Herzog, D. Kaplan, C. Spielmann, and F. Krausz, Opt. Lett. **28**, 1832 (2003).
8. H. Fattahi, H. G. Barros, M. Gorjan, T. Nubbemeyer, B. Alsaif, C. Y. Teisset, M. Schultze, S. Prinz, M. Haefner, M. Ueffing, A. Alismail, L. Vámos, A. Schwarz, O. Pronin, J. Brons, X. T. Geng, G. Arisholm, M. Ciappina, V. S. Yakovlev, D. E. Kim, A. M. Azzeer, N. Karpowicz, D. Sutter, Z. Major, T. Metzger, and F. Krausz, Optica **1**, 45 (2014).
9. G. Cerullo and S. D. Silvestri, Rev. Sci. Instrum. **74**, 1 (2003).
10. S. Witte and K. S. E. Eikema, IEEE J. Sel. Top. Quantum Electron. **18**, 296 (2012).
11. B. E. Schmidt, N. Thiré, M. Boivin, A. Laramée, F. Poitras, G. Lebrun, T. Ozaki, H. Ibrahim, and F. Légaré, Nat. Commun. **5**, 3643 (2014).
12. P. Wang, X. Shen, Z. Zeng, J. Liu, R. Li, and Z. Xu, Opt. Lett. **44**, 3952 (2019).
13. M. Sun, X. Xie, J. Zhu, X. Zhang, Y. Zhang, P. Zhu, A. Guo, J. Kang, H. Zhu, Q. Yang, and X. Liang, Appl. Opt. **60**, 2056 (2021).
14. G. Vampa, T. Hammond, M. Nesrallah, A. Y. Naumov, P. B. Corkum, and T. Brabec, Science **359**, 673 (2018).
15. M. Nesrallah, G. Vampa, G. Bart, P. B. Corkum, C. R. McDonald, and T. Brabec, Optica **5**, 271 (2018).
16. R. L. Sutherland, *Handbook of Nonlinear Optics*, 2nd ed. (Marcel Dekker, 2003).
17. P. Kabaciński, T. M. Kardaś, Y. Stepanenko, and C. Radzewicz, Opt. Express **27**, 11018 (2019).
18. R. Adair, L. L. Chase, and S. A. Payne, Phys. Rev. B **39**, 3337 (1989).
19. Y. S. You, D. A. Reis, and S. Ghimire, Nat. Phys. **13**, 345 (2016).
20. D. H. Ko, G. G. Brown, C. Zhang, and P. B. Corkum, J. Phys. B **53**, 124001 (2020).
21. A. Korobenko, T. Hammond, C. Zhang, A. Y. Naumov, D. M. Villeneuve, and P. B. Corkum, Opt. Express **27**, 32630 (2019).
22. R. Weigand and H. M. Crespo, Appl. Sci. **5**, 485 (2015).
23. T. Winkler, P. Balling, B. Zielinski, C. Sarpe, N. Jelzow, R. Ciobotea, A. Senftleben, and T. Baumert, Phys. Rev. Res. **2**, 023341 (2020).
24. K. Ekvall, C. Lundevall, and P. van der Meulen, Opt. Lett. **26**, 896 (2001).
25. V. Besse, G. Boudebs, and H. Leblond, Appl. Phys. B **116**, 911 (2014).
26. C. Schnebelin, C. Cassagne, C. B. de Araújo, and G. Boudebs, Opt. Lett. **39**, 5046 (2014).
27. S. Heo, E. Cho, H.-I. Lee, G. S. Park, H. J. Kang, T. Nagatomi, P. Choi, and B.-D. Choi, AIP Adv. **5**, 077167 (2015).
28. Y. V. Grudtsyn, A. V. Koribut, A. A. Rogashevskii, and S. L. Semjonov, Laser Phys. Lett. **17**, 075403 (2020).
29. A. D. Bristow, N. Rotenberg, and H. M. van Driel, Appl. Phys. Lett. **90**, 191104 (2007).
30. W. Chen, S. Bhaumik, S. A. Velduis, G. Xing, Q. Xu, M. Grätzel, S. Mhaisalkar, N. Mathews, and T. C. Sum, Nat. Commun. **8**, 15198 (2017).